

Large non-saturating Nernst thermopower and magnetoresistance in compensated semimetal ScSb

Antu Laha,^{1,2,*} Sarah Paone,^{1,2} Niraj Aryal,² and Qiang Li^{1,2,†}

¹*Department of Physics and Astronomy, Stony Brook University, Stony Brook, New York 11794-3800, USA*

²*Condensed Matter Physics and Materials Science Division,
Brookhaven National Laboratory, Upton, New York 11973-5000, USA*

Today, high-performance thermoelectric and thermomagnetic materials operating in the low-temperature regime, particularly below the boiling point of liquid nitrogen remain scarce. Most thermomagnetic materials reported to date exhibit a strong Nernst signal along specific crystallographic directions in their single-crystal form. However, their performance typically degrades significantly in the polycrystalline form. Here, we report an improved Nernst thermopower of $\sim 128 \mu\text{V/K}$ at 30 K and 14 T in polycrystalline compensated semimetal ScSb, in comparison to that was observed in single crystal ScSb previously. The magnetic field dependence of Nernst thermopower shows a linear and non-saturating behavior up to 14 T. The maximum Nernst power factor reaches to $\sim 240 \times 10^{-4} \text{ W m}^{-1} \text{ K}^{-2}$ and Nernst figure of merit reaches to $\sim 11 \times 10^{-4} \text{ K}^{-1}$. Polycrystalline ScSb also shows a large non-saturating magnetoresistance of $\sim 940\%$ at 2 K and 14 T. These enhanced properties originate from better electron-hole compensation, as revealed by Hall resistivity measurements. The cubic symmetry and absence of anisotropy in ScSb allow its polycrystalline form to achieve similar enhanced thermomagnetic and electromagnetic performance comparable to that of the single crystal.

I. INTRODUCTION

Thermoelectric systems enable the direct conversion of heat into electricity and vice versa, positioning them as promising technologies for applications like harvesting energy from waste heat and achieving solid-state cooling [1–4]. The efficiency of these devices in generating power is largely influenced by the power factor (PF), calculated using the formula $PF = \sigma S^2$, where σ is the electrical conductivity and S is the thermopower. Depending on how the voltage output aligns with the applied temperature gradient, two primary effects are observed: the longitudinal Seebeck effect and the transverse Nernst effect. In the Seebeck effect, the voltage is generated along the same direction as the thermal gradient. In contrast, the Nernst effect is activated in the presence of a magnetic field—producing a voltage that is perpendicular to the temperature difference. Accordingly, the power factors for these effects are represented as $PF_S = \sigma_{yy} S_{xx}^2$ for Seebeck and $PF_N = \sigma_{yy} S_{yx}^2$ for Nernst, with S_{xx} and S_{yx} denoting the Seebeck and Nernst thermopower respectively. Nernst-based thermoelectric devices offer a simpler design compared to Seebeck-based devices, as they eliminate the need for paired p-type and n-type components. This not only streamlines the fabrication process but also minimizes both thermal and electrical resistance in the final device.

Recently, topological semimetals such as Cd_3As_2 , ZrTe_5 , NbP , PtSn_4 , Mg_2Pb , NbSb_2 , and WTe_2 have emerged as exceptional candidates for enhancing the Nernst effect [5–12]. The enhancement of the Nernst

thermopower in these materials is believed to stem from the combined influence of three key mechanisms: (i) the phonon drag effect, which involves momentum transfer from lattice vibrations to charge carriers; (ii) the electron-hole compensation effect, which balances carrier populations to optimize transport; and (iii) the presence of topologically non-trivial band structures, which significantly alter the charge transport behavior in magnetic fields. Notably, these materials exhibit high thermomagnetic efficiency in their single-crystal form, with the Nernst thermopower being prominent along specific crystallographic axes. However, their performances reduced considerably in the polycrystalline form. For instance, NbP single crystals exhibit a large Nernst thermopower of $800 \mu\text{V/K}$, which drops to $90 \mu\text{V/K}$ in polycrystalline samples [13]. Polycrystalline samples are generally more suitable for device applications due to their ease of synthesis in large bulk size, whereas single crystals are limited in size by their growth methods. The reduction of the Nernst thermopower in polycrystalline materials depends on their crystal structure, as the measured value represents an average of the Nernst responses along different crystallographic directions. Materials that crystallize in a cubic structure may serve as more promising candidates, owing to the absence of crystallographic anisotropy.

The MX family of compounds ($M = \text{Sc, Y, La, Ce, Pr, Nd, Sm, Gd, Tb, Yb, Lu}$; $X = \text{As, Sb, Bi}$) crystallizes in a cubic structure and their single crystals have been extensively studied for exceptionally large non-saturating magnetoresistance driven by electron-hole compensation [14–27]. However, another intriguing phenomenon arising from electron-hole compensation - the large Nernst effect, has not yet been investigated in any member of this family except ScSb. Despite the topologically trivial electronic band structure, we recently reported a large Nernst

* antulaha.physics@gmail.com

† qiang.li@stonybrook.edu

thermopower in ScSb single crystals, due to electron-hole compensation effect. [28]. In the present work, we report both a pronounced non-saturating Nernst thermopower and a large non-saturating magnetoresistance in polycrystalline ScSb. The magnetoresistance is 940% at 2 K and 14 T. The Nernst thermopower reaches a peak value of $128 \mu\text{V/K}$ at 14 T and 30 K, resulting in a maximum Nernst power factor of $240 \times 10^{-4} \text{ W m}^{-1} \text{ K}^{-2}$, which is nearly seven times the value found in the single crystal samples at the same temperature and magnetic field [28]. The Nernst power factor for polycrystalline ScSb is even larger than that of Seebeck power factor (PF_S) found in state-of-the-art thermoelectric materials such as Bi_2Te_3 ($PF_S = 42 \times 10^{-4} \text{ W m}^{-1} \text{ K}^{-2}$) [29], PbTe ($PF_S = 25 \times 10^{-4} \text{ W m}^{-1} \text{ K}^{-2}$) [30], and SnSe ($PF_S = 10 \times 10^{-4} \text{ W m}^{-1} \text{ K}^{-2}$) [31].

II. METHODS

Polycrystalline ScSb samples were synthesized through a combined approach of solid-state reaction and spark plasma sintering (SPS). Stoichiometric amounts of Sc ingot (99.99%), and Sb chips (99.999%) were put together in an evacuated quartz ampoule, and then the ampoule was kept inside a muffle furnace at a temperature of 800°C for 72 hours to achieve a complete reaction. The reacted product was ground into fine powders, and loaded into a graphite die with inner diameter of 15 mm. The content was immediately sintered at 850°C for 15 min under an uniaxial pressure of 50 MPa using SPS. The relative density of the compacted pellet was $\sim 96\%$.

The powders of polycrystalline ScSb were characterized by x-ray diffraction (XRD) technique using $\text{Cu-K}\alpha$ radiation in a Rigaku miniflex diffractometer to determine the crystal structure and the phase purity. The XRD data were analyzed by Rietveld structural refinement using the FULLPROF package [32]. The chemical compositions were confirmed by energy dispersive x-ray spectroscopy (EDS) measurements in a JEOL JSM-7600F scanning electron microscope. Electronic transport measurements were carried out in a physical property measurement system (PPMS, Quantum Design) via the standard four-probe method. The Seebeck thermopower and Nernst thermopower were measured using four-probe technique on a standard thermal transport option (TTO) platform, and a modified one where the Cu wires for measuring voltage signals were separated from the Cernox 1050 thermometers [9].

III. RESULTS AND DISCUSSIONS

The cubic crystal structure (space group $Fm\bar{3}m$) of polycrystalline ScSb is confirmed by the Rietveld refinement of powder x-ray diffraction pattern [Fig.1(a) and 1(b)]. The low magnification scanning electron microscopy (SEM) image as shown in Fig.1(c) indicates

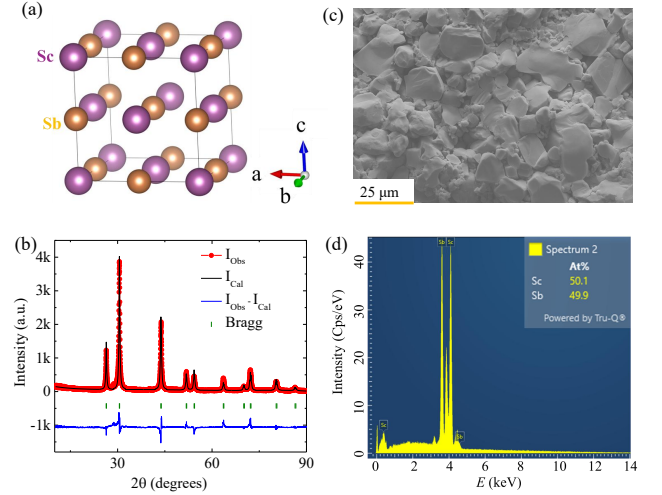


FIG. 1. (a) Cubic crystal structure of ScSb. (b) Refined powder x-ray diffraction pattern of polycrystalline ScSb, recorded at room temperature. The observed intensity (red scattered points), Rietveld refinement fit (solid black line), difference between the experimentally observed and calculated intensities (solid blue line), and Bragg peak positions (vertical green bars) are shown. (c) Low magnification scanning electron microscopy (SEM) image of fractured polycrystalline ScSb, showing the grains. (d) Energy-dispersive X-ray spectroscopy confirms the stoichiometry of the compound.

that the grain size of synthesized polycrystalline ScSb is in several microns. The EDS analysis confirms the single-phase nature and almost perfect stoichiometry of the polycrystalline sample [Fig.1(d)].

As shown in Fig. 2(a), polycrystalline ScSb exhibits a large and non-saturating magnetoresistance (MR) of $\sim 940\%$ at 2 K and 14 T. Such a high MR is atypical for polycrystalline materials. On one hand grain boundaries generally act as scattering centers that impede the motion of charge carriers, on the other hand grain boundaries can disrupt the coherent cyclotron motion of electrons and holes in magnetic fields, thereby reducing the overall MR in some cases. This grain boundary scattering effect in magnetic fields is small in conventional metal or semiconductors. However, in certain topological semimetals such as NbSb_2 and NbP , a large MR has been observed even in polycrystalline form [33, 34]. This unusual behavior is often attributed to a combination of factors: high carrier mobility enabled by linearly dispersing electronic bands, topologically protected states that reduce backscattering, and nearly perfect compensation between electron and hole carriers. These mechanisms can collectively sustain high MR despite the presence of grain boundaries. In addition, silver chalcogenides such as $\text{Ag}_{2+\delta}\text{Se}$ and $\text{Ag}_{2+\delta}\text{Te}$, have been reported to show substantial MR ($\sim 200\%$) in polycrystalline samples [35].

To investigate the origin of the large MR in ScSb, we carried out Hall resistivity (ρ_{yx}) measurements over a

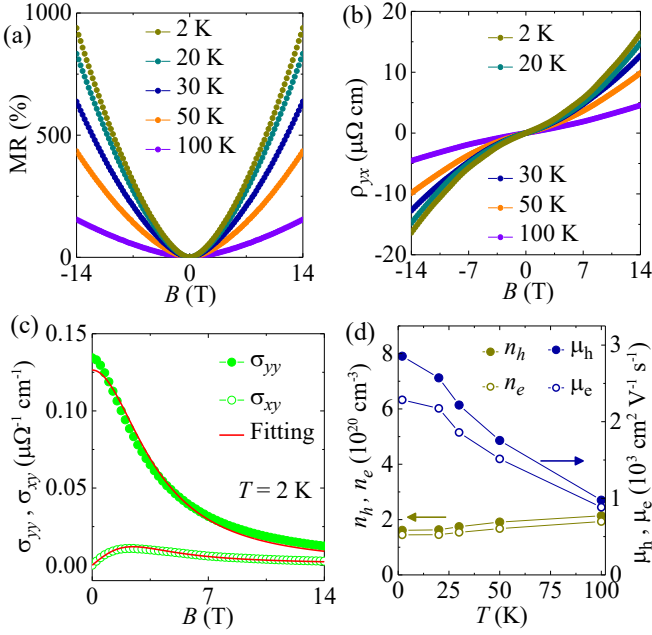


FIG. 2. (a) Longitudinal resistivity (ρ_{yy}), and (b) Hall resistivity (ρ_{yx}) as function of B at various temperatures. (c) Simultaneous fitting of longitudinal conductivity (σ_{yy}) and Hall conductivity (σ_{xy}) with two carriers model (equation (1) and (2)). (d) Hole (electron) density n_h (n_e) and mobility μ_h (μ_e) as a function of temperature.

range of temperatures [see Fig. 2(b)]. The nonlinear field dependence of ρ_{yx} is indicative of multi-carrier transport, with both electrons and holes contributing to conduction. To quantify their respective densities and mobilities, we consider a semiclassical two-carrier model to simultaneously fit the Hall conductivity (σ_{xy}) and longitudinal conductivity (σ_{yy}) as shown in Fig. 2(c). According to semiclassical two-carrier model [36, 37], the σ_{yy} and σ_{xy} can be expressed as

$$\sigma_{yy} = e \left[\frac{n_h \mu_h}{1 + \mu_h^2 B^2} + \frac{n_e \mu_e}{1 + \mu_e^2 B^2} \right] \quad (1)$$

$$\sigma_{xy} = eB \left[\frac{n_h \mu_h^2}{1 + \mu_h^2 B^2} - \frac{n_e \mu_e^2}{1 + \mu_e^2 B^2} \right] \quad (2)$$

where n_h (n_e) and μ_h (μ_e) are the hole (electron) density and mobility, respectively. The σ_{yy} and σ_{xy} are obtained using the expressions $\sigma_{yy} = \frac{\rho_{yy}}{\rho_{yy}^2 + \rho_{yx}^2}$, and $\sigma_{xy} = \frac{\rho_{yx}}{\rho_{yy}^2 + \rho_{yx}^2}$. The calculated carrier densities (error bar: $\pm 5\%$) and mobilities (error bar: $\pm 5\%$) from the two carriers model fitting are plotted as a function of temperature in Fig. 2(d). The low carrier density of $\sim 1.5 \times 10^{20} \text{ cm}^{-3}$ suggests a semimetallic nature of the polycrystalline sample. The carrier density ratio (n_h/n_e is ~ 1.1) indicates the occurrence of electron-hole compensation. This, combined with the high carrier mobility

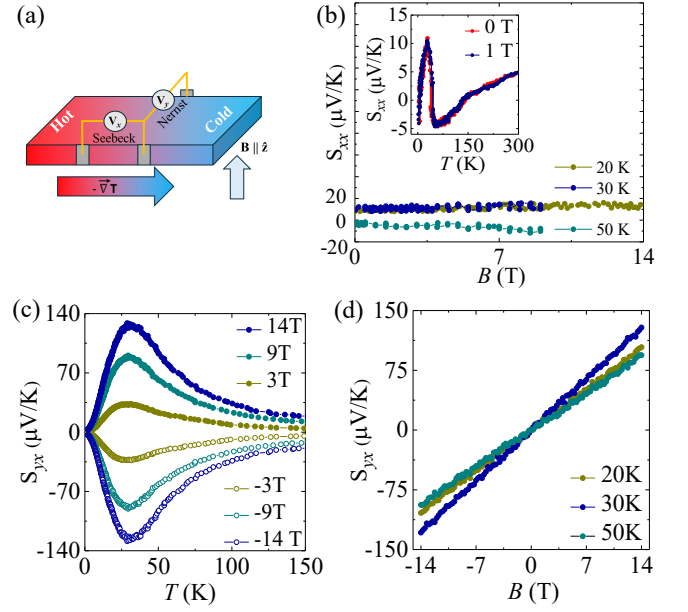


FIG. 3. (a) Schematic diagram for Seebeck and Nernst effect measurements. (b) Seebeck thermopower (S_{xx}) as a function of magnetic field. The inset shows temperature dependence of S_{xx} . (c) Nernst thermopower (S_{yx}) as a function of temperature at various magnetic fields. (d) Nernst thermopower as function of magnetic field at various temperatures.

TABLE I. Comparison of maximum Nernst thermopower (S_{yx}), hole-to-electron density ratio (n_h/n_e), and effective mobility ($\mu = \sqrt{\mu_h \mu_e}$) between single-crystal (ref. [28]) and polycrystalline sample (this work) of ScSb.

ScSb	$S_{yx} (\mu\text{V/K})$	n_h/n_e	$\mu (\text{cm}^2 \text{V}^{-1} \text{s}^{-1})$
Single-crystal	~ 47 (12 K, 14 T)	0.8	2210 (2 K)
Polycrystalline	~ 128 (30 K, 14 T)	1.1	2553 (2 K)

($\mu = \sqrt{\mu_h \mu_e}$) of $\sim 2553 \text{ cm}^2 \text{V}^{-1} \text{s}^{-1}$ at 2 K, is primarily responsible for the large non-saturating magnetoresistance observed in polycrystalline ScSb.

Seebeck thermopower (S_{xx}) and Nernst thermopower (S_{yx}) are measured as a function of temperature for polycrystalline ScSb as shown in Fig. 3(b) and 3(c). The S_{xx} in polycrystalline ScSb is positive in the temperature range 135 K – 300 K, shows a crossover from positive to negative at ~ 135 K and another crossover from negative to positive at ~ 42 K as shown in the inset of Fig. 3(b). This behavior indicates that the sample is very close to electron-hole compensation. In contrast, single-crystal ScSb shows negative S_{xx} between 100 K and 300 K, with a single crossover from negative to positive at ~ 100 K [28]. The S_{xx} in polycrystalline ScSb shows a strong peak of $\sim 10 \mu\text{V/K}$ at ~ 30 K. In ScSb single crystal, a similar peak has been observed at 12 K with a value of $\sim 2.8 \mu\text{V/K}$. A distinct peak in the longitudinal Seebeck coefficient (S_{xx}) is a well-known feature in many thermoelectric and thermomagnetic materials

TABLE II. Parameters used to fit the measured thermal conductivity of polycrystalline ScSb.

T (K)	κ_l ($\text{W K}^{-1} \text{m}^{-1}$)	κ_e ($\text{W K}^{-1} \text{m}^{-1}$)	η (T^{-s})	s
20	9.88	12.88	0.58	1.32
30	20.87	8.39	0.39	1.05
50	27.24	8.56	0.37	1.49

and is typically attributed to the phonon-drag mechanism. As temperature increases, phonons with higher momentum become thermally activated. When these long-wavelength acoustic phonons transfer their momentum efficiently to charge carriers near the Fermi surface, a drag effect arises, producing an enhancement in thermopower at low temperatures [9, 34, 38, 39]. Notably, the temperature dependence of $S_{xx}(T)$ at zero field and under an applied magnetic field of 1 T overlaps throughout the entire temperature range from 2 K to 300 K, as shown in the inset of Fig.3(b). Furthermore, we measured the magnetic field dependence of S_{xx} at several temperatures as shown in Fig.3(b). The S_{xx} remains nearly unchanged with increasing magnetic field.

Fig. 3(c) shows the transverse thermopower (S_{yx}), or Nernst signal, as a function of temperature at various magnetic fields. A pronounced peak appears around 30 K, similar to that observed in S_{xx} , which is attributed to the phonon drag effect. This peak becomes more significant under stronger magnetic fields, reaching $\sim 128 \mu\text{V/K}$ at 14 T. When the magnetic field is reversed to -14 T, S_{yx} exhibits a similar trend but with an opposite sign, consistent with antisymmetric Nernst response. Large Nernst thermopower has previously been reported in several topological semimetals, where it is often attributed to the combined effects of non-trivial band topology and near-perfect electron-hole compensation. Interestingly, in the case of polycrystalline ScSb, a material with topologically trivial electronic bands, we also observe a significant enhancement of the Nernst effect, suggesting that electron-hole compensation alone can lead to substantial thermomagnetic response. The observed S_{yx} in polycrystalline ScSb is larger than that of its single-crystalline counterpart ($S_{yx} \sim 35 \mu\text{V/K}$ at 12 K and 14 T) [28], likely due to improved electron-hole compensation. A comparison of the Nernst thermopower, hole-to-electron density ratio, and carrier mobility between polycrystalline and single-crystalline ScSb is presented in table I. The peak value of S_{yx} in polycrystalline ScSb is comparable to that of polycrystalline Mg_3Bi_2 ($127 \mu\text{V/K}$ at 13.5 T and 15 K) [40], and even exceeds that seen in other polycrystalline thermomagnetic compounds such as NbP ($90 \mu\text{V/K}$ at 9 T and 136 K) [13], $\text{Bi}_{77}\text{Sb}_{23}$ ($88.5 \mu\text{V/K}$ at 6 T and 50 K) [41], Te-doped $\text{Bi}_{77}\text{Sb}_{23}$ ($45 \mu\text{V/K}$ at 6 T and 200 K) [41] and $\text{Ag}_{2(1+x)}\text{Se}$ ($15 \mu\text{V/K}$ 5 T and 300 K) [42].

The S_{yx} linearly increases with increasing magnetic fields, without showing a signature of saturation up to

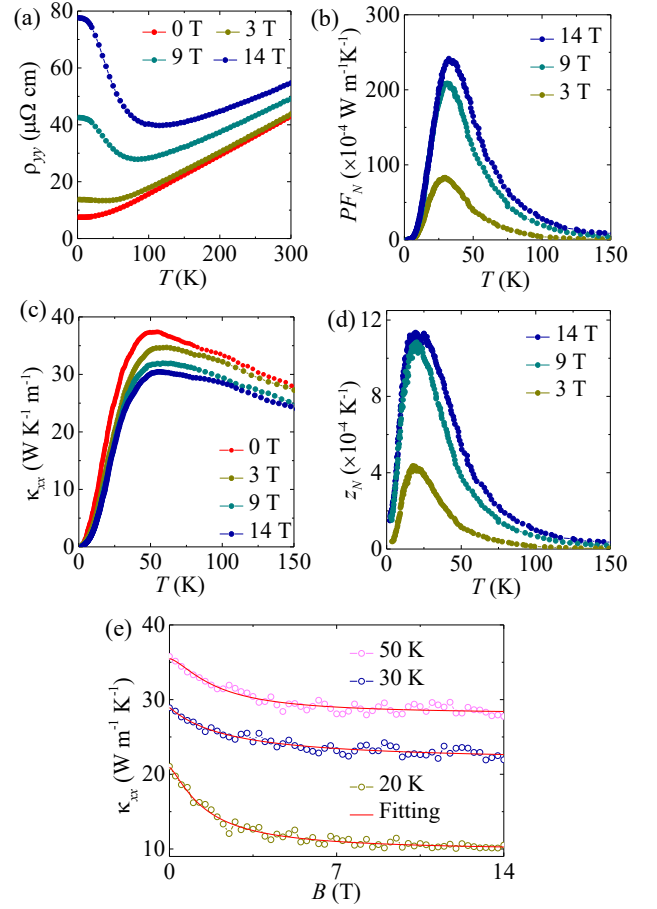


FIG. 4. (a) Longitudinal electrical resistivity (ρ_{yy}), (b) Longitudinal thermal conductivity (κ_{xx}), (c) Nernst power factor (PF_N), and (d) Nernst figure of merit (z_N) as a function of temperature. (e) Measured thermal conductivity as a function of magnetic field at different temperatures. The symbols are experimental data and the lines are the fitting curves to the equation (5) [fitting error : $\pm 10\%$].

14 T as shown in Fig.3(d). Such a non-saturating S_{yx} is previously reported in topological semimetal such as NbSb_2 [9, 34], and it is highly uncommon in topologically trivial materials. In general, Nernst thermopower saturates at high magnetic fields in conventional metals. Since, charge carriers are confined to tight cyclotron orbits at high magnetic fields, limiting their transverse motion and causing the thermoelectric response to stop increasing with further increases in field. To understand the linear non-saturating S_{yx} in ScSb, we consider the two carriers model for electronic and thermal transport. When both the electrons and holes take part in electrical transports, the S_{yx} can be expressed as [12, 39]

$$S_{yx} = \frac{\sigma_{yy}^e \sigma_{yy}^h (\mu_e + \mu_h) B}{(\sigma_{yy}^e + \sigma_{yy}^h)^2 + (\sigma_{yy}^e \mu_e B - \sigma_{yy}^h \mu_h B)^2} (S_{xx}^h - S_{xx}^e) \quad (3)$$

When the magnetic field is weak ($\mu B \ll 1$), the electrical conductivity dominates the denominator, causing S_{yx} to

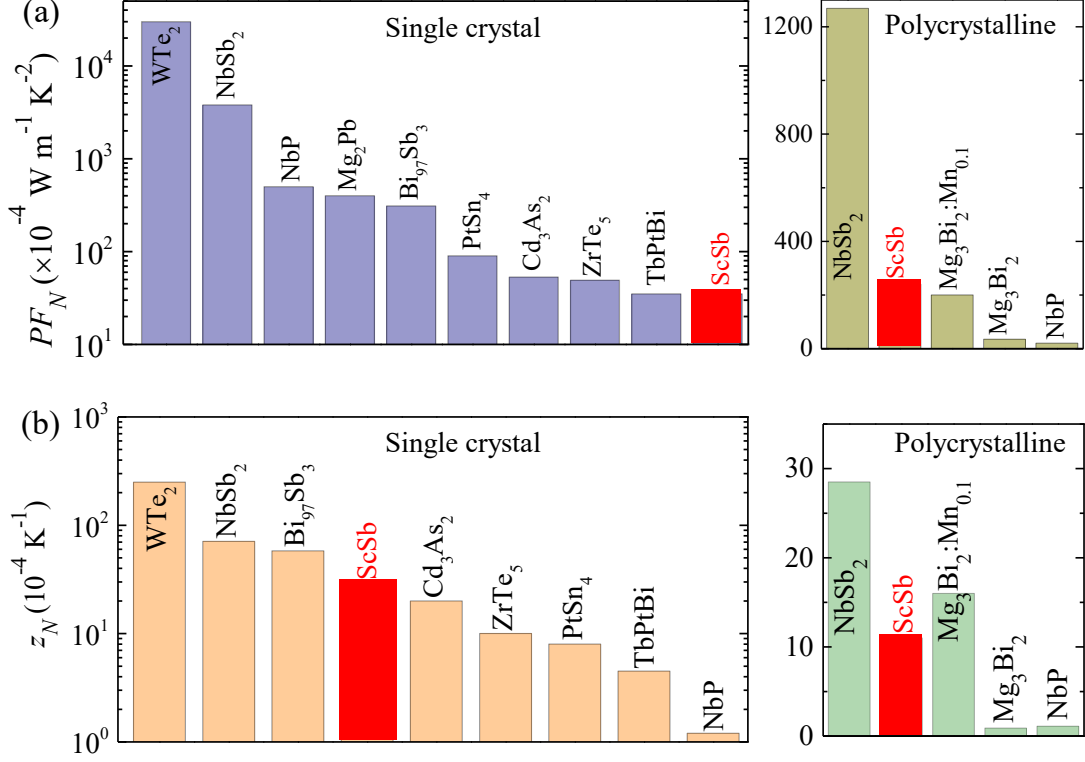


FIG. 5. Comparison of the maximum (a) Nernst power factor PF_N and (b) Nernst figure of merit z_N of ScSb and other thermomagnetic materials [5–9, 11, 28, 33, 34, 40, 43–47].

grow linearly with increasing B . In contrast, under a strong magnetic field ($\mu B \gg 1$), S_{yx} becomes inversely proportional to B if the electron and hole contributions to the Hall conductivity are significantly unbalanced. In the idealized scenario where the carrier concentrations and mobilities are equal for electrons and holes, $n_e = n_h = n$ and $\mu_e = \mu_h = \mu$, their Hall effects cancel each other out, producing the maximum possible thermomagnetic response. In this case, S_{yx} can be reformulated as

$$S_{yx} = \frac{S_{xx}^h - S_{xx}^e}{2} \mu B \quad (4)$$

For polycrystalline ScSb, $n_h/n_e \sim 1.1$ and $\mu_h/\mu_e \sim 1.2$, indicating a nearly ideal scenario for maximum thermomagnetic response, which leads to a linear non-saturating S_{yx} even at high magnetic fields of 14 T.

To determine the Nernst power factor (PF_N) and Nernst figure of merit (z_N), we measured the longitudinal electrical conductivity (σ_{yy}) and longitudinal thermal conductivity (κ_{xx}) as shown in Fig.4(a) and 4(c). As the temperature increases, the κ_{xx} initially rises, reaching a peak around 50K, and then decreases at higher temperatures. Such a peak has also been reported in several topological thermomagnetic materials exhibiting a large Nernst effect, including NbP and NbSb₂ [13, 34]. The peak value of κ_{xx} in polycrystalline ScSb is $\sim 37 \text{ W K}^{-1} \text{ m}^{-1}$ (at 50 K), which is smaller than the peak value observed in polycrystalline NbP ($\sim 65 \text{ W K}^{-1} \text{ m}^{-1}$ at

85 K) and NbSb₂ ($\sim 90 \text{ W K}^{-1} \text{ m}^{-1}$ at 35 K) [13, 34]. Under an applied magnetic field, κ_{xx} exhibits a significant reduction, decreasing to $\sim 30 \text{ W K}^{-1} \text{ m}^{-1}$ at 14 T in polycrystalline ScSb. The measured κ_{xx} in Fig.4(c) is composed of the lattice thermal conductivity κ_l and electronic thermal conductivity κ_e . Under magnetic field, their relationship can be expressed by the empirical formula [9, 34, 48],

$$\kappa_{xx}(B, T) = \kappa_l(T) + \kappa_e(B, T) = \kappa_l(T) + \frac{\kappa_e(0, T)}{1 + \eta B^s} \quad (5)$$

where η and s are the two factors related to the thermal mobility and scattering mechanism, respectively. The increase of B will suppress the contribution of carriers, which is responsible for the reduction of κ_{xx} under high magnetic field (Fig.4(c)). By using the above equation, the measured κ_{xx} data of ScSb under different B and T are fitted. The fitting results are shown in Fig.4(e) and table II. The electronic thermal conductivity estimated from the the Wiedemann–Franz law, $\kappa_e = L_0 \sigma_{yy} T$, is $\sim 12.2 \text{ W K}^{-1} \text{ m}^{-1}$ at 50 K, where $L_0 = 2.44 \times 10^{-8} \text{ W } \Omega \text{ K}^{-2}$. This value exceeds the actual κ_e ($\sim 8.56 \text{ W K}^{-1} \text{ m}^{-1}$) obtained from fitting equation (5) to the measured thermal conductivity κ_{xx} . This discrepancy indicates a violation of the Wiedemann–Franz law, possibly due to inelastic scattering of the charge carriers under a strong magnetic field, and such a violation has also been re-

ported in NbSb₂ and WP₂ [9, 34, 49, 50].

The Nernst power factor and Nernst figure of merit are calculated using the relations $PF_N = S_{yx}^2/\rho_{yy}$ and $z_N = S_{yx}^2/(\rho_{yy} \kappa_{xx})$ as displayed in Fig.4(b) and 4(d). In polycrystalline ScSb, PF_N reaches a maximum of $\sim 240 \times 10^{-4} \text{ W m}^{-1} \text{ K}^{-2}$ at 30 K and 14 T, which is significantly higher than the value for single-crystalline ScSb ($\sim 35 \times 10^{-4} \text{ W m}^{-1} \text{ K}^{-2}$ at 12 K and 14 T) [28]. Furthermore, this PF_N exceeds the Seebeck power factors (PF_S) of state-of-the-art thermoelectric materials such as Bi₂Te₃ ($PF_S = 42 \times 10^{-4} \text{ W m}^{-1} \text{ K}^{-2}$) [29], CoSb₃ ($PF_S = 40 \times 10^{-4} \text{ W m}^{-1} \text{ K}^{-2}$) [51], PbTe ($PF_S = 25 \times 10^{-4} \text{ W m}^{-1} \text{ K}^{-2}$) [30], and SnSe ($PF_S = 10 \times 10^{-4} \text{ W m}^{-1} \text{ K}^{-2}$) [31]. Despite ScSb's trivial electronic band structure, the maximum PF_N in polycrystalline ScSb surpasses that of several topological semimetals, including single-crystalline Cd₃As₂, ZrTe₅, PtSn₄ and TbPtBi [5–7, 45], as well as polycrystalline NbP and Mg₃Bi₂ [13, 40]. The peak values of PF_N and z_N for polycrystalline ScSb are compared with those of various topological thermomagnetic single crystals and polycrystalline materials in Fig.5.

IV. CONCLUSIONS

The tunability of the Nernst thermopower in ScSb primarily depends on electron-hole compensation, with the highest S_{yx} achieved at perfect compensation ($n_h/n_e = 1$). In ScSb single crystals, the Fermi level varies from crystal to crystal, resulting in either electron or hole doping, and consequently, deviations from perfect electron-hole compensation. This variability is reflected in the

magnetoresistance of ScSb single crystals, which ranges from $\sim 500\%$ to $\sim 28000\%$ depending on the individual crystal [14]. Controlling the level of electron or hole doping is particularly challenging in single crystals, as they are typically grown using excess Sb flux. In contrast, polycrystalline samples offer an advantage, as they are synthesized using an exact stoichiometric ratio of the constituent elements. Our polycrystalline ScSb shows a larger S_{yx} ($\sim 128 \mu\text{V/K}$ at 30 K and 14 T) compared to its single-crystalline counterpart ($S_{yx} \sim 35 \mu\text{V/K}$ at 12 K and 14 T) [28], likely due to improved electron-hole compensation. Polycrystalline ScSb also shows a large non-saturating magnetoresistance of $\sim 940\%$ at 2 K and 14 T. The cubic crystal structure provides an advantage in achieving enhanced thermomagnetic and electromagnetic performance in polycrystalline form, comparable to that of single crystals. Such behavior has been observed in the cubic topological thermomagnetic material Co₂MnGa [52]. In contrast, other crystal structures such as tetragonal tend to exhibit a reduced average S_{yx} in their polycrystalline forms. For example, while NbP single crystals show a large Nernst thermopower of $800 \mu\text{V/K}$, it drops sharply to $90 \mu\text{V/K}$ in polycrystalline samples [13]. Further enhancement of the Nernst effect in ScSb may be achieved by precisely tuning the electron-hole composition.

ACKNOWLEDGMENTS

The research at Brookhaven National Laboratory was supported by the U.S. Department of Energy, Office of Basic Energy Sciences, Contract No. DE-SC0012704.

-
- [1] L. E. Bell, Cooling, heating, generating power, and recovering waste heat with thermoelectric systems, *Science* **321**, 1457 (2008).
 - [2] R. Funahashi, L. Chen, E. Guilmeau, Q. Li, M. Gao, and Y. Miyazaki, eds., *Thermoelectric Energy Conversion – Theories and Mechanisms, Materials, Devices, and Applications*, 1st ed. (Elsevier, 2021).
 - [3] G. J. Snyder and E. S. Toberer, Complex thermoelectric materials, *Nature Materials* **7**, 105 (2008).
 - [4] J. Mao, G. Chen, and Z. Ren, Thermoelectric cooling materials, *Nature Materials* **20**, 454 (2021).
 - [5] T. Liang, J. Lin, Q. Gibson, T. Gao, M. Hirschberger, M. Liu, R. J. Cava, and N. P. Ong, Anomalous nernst effect in the Dirac semimetal Cd₃As₂, *Phys. Rev. Lett.* **118**, 136601 (2017).
 - [6] P. Wang, C.-w. Cho, F. Tang, P. Wang, W. Zhang, M. He, G. Gu, X. Wu, Y. Shao, and L. Zhang, Giant Nernst effect and field-enhanced transversal $z_N T$ in ZrTe₅, *Phys. Rev. B* **103**, 045203 (2021).
 - [7] C. Fu, S. N. Guin, T. Scaffidi, Y. Sun, R. Saha, S. J. Watzman, A. K. Srivastava, G. Li, W. Schnelle, S. S. P. Parkin, C. Felser, and J. Gooth, Largely suppressed magneto-thermal conductivity and enhanced magneto-thermoelectric properties in PtSn₄, *Research* **2020** (2020).
 - [8] Z. Chen, X. Zhang, J. Ren, Z. Zeng, Y. Chen, J. He, L. Chen, and Y. Pei, Leveraging bipolar effect to enhance transverse thermoelectricity in semimetal Mg₂Pb for cryogenic heat pumping, *Nature Communications* **12**, 3837 (2021).
 - [9] P. Li, P. Qiu, Q. Xu, J. Luo, Y. Xiong, J. Xiao, N. Aryal, Q. Li, L. Chen, and X. Shi, Colossal Nernst power factor in topological semimetal NbSb₂, *Nature Communications* **13**, 7612 (2022).
 - [10] K. G. Rana, F. K. Dejene, N. Kumar, C. R. Rajamathi, K. Sklarek, C. Felser, and S. S. P. Parkin, Thermopower and unconventional Nernst effect in the predicted type-ii Weyl semimetal WTe₂, *Nano Letters* **18**, 6591 (2018).
 - [11] Y. Pan, B. He, T. Helm, D. Chen, W. Schnelle, and C. Felser, Ultrahigh transverse thermoelectric power factor in flexible weyl semimetal WTe₂, *Nature Communications* **13**, 3909 (2022).
 - [12] P. Li, B. Jiang, P. Qiu, and X. Shi, Thermomagnetic properties in topological materials, *Advanced Functional Materials*, 2506631 (2025).

- [13] C. Fu, S. N. Guin, S. J. Watzman, G. Li, E. Liu, N. Kumar, V. Sü, W. Schnelle, G. Auffermann, C. Shekhar, Y. Sun, J. Gooth, and C. Felser, Large Nernst power factor over a broad temperature range in polycrystalline weyl semimetal NbP, *Energy Environ. Sci.* **11**, 2813 (2018).
- [14] Y. J. Hu, E. I. P. Aulestia, K. F. Tse, C. N. Kuo, J. Y. Zhu, C. S. Lue, K. T. Lai, and S. K. Goh, Extremely large magnetoresistance and the complete determination of the fermi surface topology in the semimetal ScSb, *Phys. Rev. B* **98**, 035133 (2018).
- [15] F. F. Tafti, Q. D. Gibson, S. K. Kushwaha, N. Hal-dolaarachchige, and R. J. Cava, Resistivity plateau and extreme magnetoresistance in LaSb, *Nat. Phys.* **12**, 272 (2015), article.
- [16] L. Ye, T. Suzuki, C. R. Wicker, and J. G. Checkelsky, Extreme magnetoresistance in magnetic rare-earth mononictides, *Phys. Rev. B* **97**, 081108 (2018).
- [17] C. Q. Xu, B. Li, M. R. van Delft, W. H. Jiao, W. Zhou, B. Qian, N. D. Zhigadlo, D. Qian, R. Sankar, N. E. Hussey, and X. Xu, Extreme magnetoresistance and pressure-induced superconductivity in the topological semimetal candidate YBi, *Phys. Rev. B* **99**, 024110 (2019).
- [18] S. Xiao, Y. Li, Y. Li, X. Yang, S. Zhang, W. Liu, X. Wu, B. Li, M. Arita, K. Shimada, Y. Shi, and S. He, Direct evidence of electron-hole compensation for extreme magnetoresistance in topologically trivial YBi, *Phys. Rev. B* **103**, 115119 (2021).
- [19] O. Pavlosiuk, P. Swatek, and P. Wisniewski, Giant magnetoresistance, three-dimensional fermi surface and origin of resistivity plateau in YSb semimetal, *Sci. Rep.* **6**, 38691 (2016), article.
- [20] W. Xie, Y. Wu, F. Du, A. Wang, H. Su, Y. Chen, Z. Y. Nie, S.-K. Mo, M. Smidman, C. Cao, Y. Liu, T. Takabatake, and H. Q. Yuan, Magnetotransport and electronic structure of the antiferromagnetic semimetal YbAs, *Phys. Rev. B* **101**, 085132 (2020).
- [21] F. Wu, C. Y. Guo, M. Smidman, J. L. Zhang, and H. Q. Yuan, Large magnetoresistance and fermi surface topology of PrSb, *Phys. Rev. B* **96**, 125122 (2017).
- [22] Z. Wu, F. Wu, P. Li, C. Guo, Y. Liu, Z. Sun, C.-M. Cheng, T.-C. Chiang, C. Cao, H. Yuan, and Y. Liu, Probing the origin of extreme magnetoresistance in Pr/Sm mono-antimonides/bismuthides, *Phys. Rev. B* **99**, 035158 (2019).
- [23] N. Wakeham, E. D. Bauer, M. Neupane, and F. Ronning, Large magnetoresistance in the antiferromagnetic semimetal NdSb, *Phys. Rev. B* **93**, 205152 (2016).
- [24] Z. Zhao, X. Guo, W. Xie, X. Li, and Z. Zhu, Large magnetoresistance, quantum oscillations, and fermi surface of compensated NdBi, *Phys. Rev. B* **111**, 115148 (2025).
- [25] G. Dwari, S. Sasmal, S. Dan, B. Maity, V. Saini, R. Kulkarni, S. Banik, R. Verma, B. Singh, and A. Thamizhavel, Large unsaturated magnetoresistance and electronic structure studies of single-crystal GdBi, *Phys. Rev. B* **107**, 235117 (2023).
- [26] O. Pavlosiuk, P. Swatek, D. Kaczorowski, and P. Wiśniewski, Magnetoresistance in LuBi and YBi semimetals due to nearly perfect carrier compensation, *Phys. Rev. B* **97**, 235132 (2018).
- [27] F. Tang, X. Shen, J. Zhou, S. Cong, L. Zhang, W. Zhou, Z.-D. Han, B. Qian, X.-F. Jiang, R.-K. Zheng, W. Zhao, X.-C. Kan, J. Tang, Y.-Y. Han, X.-Q. Yin, Y. Fang, and S. Ju, Anisotropic large magnetoresistance and fermi surface topology of terbium monoantimonide, *Materials Today Physics* **24**, 100657 (2022).
- [28] A. Laha, S. Paone, A. K. Kundu, J. Yao, N. Aryal, E. Vescovo, and Q. Li, Nernst power factor and figure of merit in compensated semimetal ScSb, [arXiv:2504.15450 \[cond-mat.mtrl-sci\]](https://arxiv.org/abs/2504.15450) (2025).
- [29] B. Poudel, Q. Hao, Y. Ma, Y. Lan, A. Minnich, B. Yu, X. Yan, D. Wang, A. Muto, D. Vashaee, X. Chen, J. Liu, M. S. Dresselhaus, G. Chen, and Z. Ren, High-thermoelectric performance of nanostructured bismuth antimony telluride bulk alloys, *Science* **320**, 634 (2008).
- [30] Y. Pei, X. Shi, A. LaLonde, H. Wang, L. Chen, and G. J. Snyder, Convergence of electronic bands for high performance bulk thermoelectrics, *Nature* **473**, 66 (2011).
- [31] L.-D. Zhao, S.-H. Lo, Y. Zhang, H. Sun, G. Tan, C. Uher, C. Wolverton, V. P. Dravid, and M. G. Kanatzidis, Ultra-low thermal conductivity and high thermoelectric figure of merit in SnSe crystals, *Nature* **508**, 373 (2014).
- [32] J. Rodríguez-Carvajal, Recent advances in magnetic structure determination by neutron powder diffraction, *Physica B: Condensed Matter* **192**, 55 (1993).
- [33] W. Liu, Z. Wang, J. Wang, H. Bai, Z. Li, J. Sun, X. Zhou, J. Luo, W. Wang, C. Zhang, J. Wu, Y. Sun, Z. Zhu, Q. Zhang, and X. Tang, Weyl semimetal states generated extraordinary quasi-linear magnetoresistance and nernst thermoelectric power factor in polycrystalline NbP, *Advanced Functional Materials* **32**, 2202143 (2022).
- [34] P. Li, P. Qiu, J. Xiao, T. Deng, L. Chen, and X. Shi, A giant Nernst power factor and figure-of-merit in polycrystalline NbSb₂ for Ettingshausen refrigeration, *Energy Environ. Sci.* **16**, 3753 (2023).
- [35] R. Xu, A. Husmann, T. F. Rosenbaum, M.-L. Saboungi, J. E. Enderby, and P. B. Littlewood, Large magnetoresistance in non-magnetic silver chalcogenides, *Nature* **390**, 57 (1997).
- [36] C. M. Hurd, *The Hall Effect in Metals and Alloys* (Plenum Press, New York) [10.1007/978-1-4757-0465-5](https://doi.org/10.1007/978-1-4757-0465-5) (1972).
- [37] C.-L. Zhang, Z. Yuan, Q.-D. Jiang, B. Tong, C. Zhang, X. C. Xie, and S. Jia, Electron scattering in tantalum monoarsenide, *Phys. Rev. B* **95**, 085202 (2017).
- [38] H. J. Goldsmid, *Thermoelectric Refrigeration*, (Plenum Press) [10.1007/978-1-4899-5723-8](https://doi.org/10.1007/978-1-4899-5723-8) (1964).
- [39] R. T. Delves, Figure of merit for ettingshausen cooling, *British Journal of Applied Physics* **15**, 105 (1964).
- [40] T. Feng, P. Wang, Z. Han, L. Zhou, W. Zhang, Q. Liu, and W. Liu, Large transverse and longitudinal magneto-thermoelectric effect in polycrystalline nodal-line semimetal Mg₃Bi₂, *Advanced Materials* **34**, 2200931 (2022).
- [41] M. Murata, K. Nagase, K. Aoyama, and A. Yamamoto, Enhancement of figure of merit for Nernst effect in Bi₇₇Sb₂₃ alloy by Te-doping, *Applied Physics Letters* **117**, 103903 (2020).
- [42] The electronic-thermal transport properties and the exploration of magneto-thermoelectric properties and the Nernst thermopower of Ag_{2(1+x)}Se, *Journal of Solid State Chemistry* **288**, 121453 (2020).
- [43] U. Stockert, R. D. dos Reis, M. O. Ajeesh, S. J. Watzman, M. Schmidt, C. Shekhar, J. P. Heremans, C. Felser, M. Baenitz, and M. Nicklas, Thermopower and thermal conductivity in the Weyl semimetal NbP, *Journal of Physics: Condensed Matter* **29**, 325701 (2017).

- [44] R. D. dos Reis, S. C. Wu, Y. Sun, M. O. Ajeesh, C. Shekhar, M. Schmidt, C. Felser, B. Yan, and M. Nicklas, Pressure tuning the fermi surface topology of the Weyl semimetal NbP, [Phys. Rev. B **93**, 205102 \(2016\)](#).
- [45] H. Wang, Z. Zhou, J. Ying, Z. Xiang, R. Wang, A. Wang, Y. Chai, M. He, X. Lu, G. Han, Y. Pan, G. Wang, X. Zhou, and X. Chen, Large magneto-transverse and longitudinal thermoelectric effects in the magnetic Weyl semimetal TbPtBi, [Advanced Materials **35**, 2206941 \(2023\)](#).
- [46] K. Vandaele, B. He, P. Van Der Voort, K. De Buysser, and J. P. Heremans, Wet-chemical synthesis of enhanced-thermopower $\text{Bi}_{1-x}\text{Sb}_x$ nanowire composites for solid-state active cooling of electronics, [Phys. Rev. Appl. **9**, 024020 \(2018\)](#).
- [47] J. Mao, H. Zhu, Z. Ding, Z. Liu, G. A. Gamage, G. Chen, and Z. Ren, High thermoelectric cooling performance of n-type Mg_3Bi_2 -based materials, [Science **365**, 495 \(2019\)](#).
- [48] R. Ocaña and P. Esquinazi, Thermal conductivity tensor in $\text{YBa}_2\text{Cu}_3\text{O}_{7-x}$: effects of a planar magnetic field, [Phys. Rev. B **66**, 064525 \(2002\)](#).
- [49] J. Gooth, F. Menges, N. Kumar, V. Süß, C. Shekhar, Y. Sun, U. Drechsler, R. Zierold, C. Felser, and B. Gotsmann, Thermal and electrical signatures of a hydrodynamic electron fluid in tungsten diphosphide, [Nature Communications **9**, 4093 \(2018\)](#).
- [50] A. Jaoui, B. Fauqué, C. W. Rischau, A. Subedi, C. Fu, J. Gooth, N. Kumar, V. Süß, D. L. Maslov, C. Felser, and K. Behnia, Departure from the Wiedemann–Franz law in WP_2 driven by mismatch in t-square resistivity prefactors, [npj Quantum Materials **3**, 64 \(2018\)](#).
- [51] Y. Tang, Z. M. Gibbs, L. A. Agapito, G. Li, H.-S. Kim, M. B. Nardelli, S. Curtarolo, and G. J. Snyder, Convergence of multi-valley bands as the electronic origin of high thermoelectric performance in CoSb_3 skutterudites, [Nature Materials **14**, 1223 \(2015\)](#).
- [52] M. Chen, J. Wang, K. Liu, W. Fan, Y. Sun, C. Felser, T. Zhu, and C. Fu, Topological heusler magnets-driven high-performance transverse Nernst thermoelectric generators, [Advanced Energy Materials **14**, 2400411 \(2024\)](#).